Key Points:
- In asymmetric reconnection, the magnetic energy is mainly converted to electrons (ions) at the electron (ion) diffusion region scale
- Reconnection electric fields (E) dominate over in-plane E in energizing electrons in the diffusion region
- The relative importance between reconnection and in-plane E for energizing ions depends on the reconnection phase

Energy Conversion and Partition in the Asymmetric Reconnection Diffusion Region

Shan Wang[1,2] iD, **Li-Jen Chen**[1,2] iD, **Naoki Bessho**[1,2] iD, **Michael Hesse**[3,4] iD, **Jongsoo Yoo**[5] iD, **Masaaki Yamada**[5], **Yi-Hsin Liu**[6] iD, **Danial J. Gershman**[2] iD, **Barbara L. Giles**[2] iD, and **Thomas E. Moore**[2] iD

[1]Astronomy Department, University of Maryland, College Park, MD, USA, [2]NASA Goddard Space Flight Center, Greenbelt, MD, USA, [3]Department of Physics and Technology, University of Bergen, Bergen, Norway, [4]Southwest Research Institute San Antonio, San Antonio, TX, USA, [5]Princeton Plasma Physics Laboratory, Princeton, NJ, USA, [6]Dartmouth College, Hanover, NH, USA

Abstract We investigate the energy conversion and partition in the asymmetric reconnection diffusion region using two-dimensional particle-in-cell simulations and Magnetosphere Multiscale (MMS) mission observations. Under an upstream condition with equal temperatures in the two inflow regions, the simulation analysis indicates that the energy partition between ions and electrons depends on the distance from the X-line. Within the central electron diffusion region (EDR), nearly all dissipated electromagnetic field energies are converted to electrons. From the EDR to the ion diffusion region (IDR) scales, the rate of the electron energy gain decreases to be lower than that of ions. A magnetopause reconnection event inside the IDR observed by MMS shows comparable ion and electron energy gains, consistent with the simulation result in the transition region from EDR to IDR. At the EDR scale, the electron energization is mainly by the reconnection electric field (E_r); in-plane electric fields (E_{xz}) provide additional positive contributions near the X-line and do negative work on electrons beyond the EDR. The guide field reduces the electron energization by both E_r and E_{xz} in the EDR. For ion energization, E_r and E_{xz} have comparable contributions near the time of the peak reconnection rate, while E_{xz} dominants at later time. At the IDR scale, the guide field causes asymmetry in the amount of the energy gain and energization mechanisms between two exhausts but does not have significant effects on energy partition. Our study advances understanding of ion and electron energization in asymmetric reconnect IDRs.

1. Introduction

Magnetic reconnection is a process that converts the electromagnetic energy to the kinetic energy of plasmas. One important question is how much of the input electromagnetic energy can be converted to particles and how the energy is partitioned between different energy forms. Simulations suggested that the outflowing enthalpy flux (representing the thermal energy gain) dominates over the bulk flow energy flux during reconnection, for symmetric reconnection with zero guide field (Aunai et al., 2011a; Birn & Hesse, 2005; Lu et al., 2013, 2018) and finite guide field (Birn & Hesse, 2010), and asymmetric reconnection with zero guide field (Aunai et al., 2011a; Birn et al., 2010).

Recent studies distinguished the energy gain by ions and electrons and found that typically the dissipated energy partitioned to ions is greater than that to electrons. Magnetopause observations in reconnection far exhausts suggested that the ion thermal energy gain relative to the inflowing electromagnetic energy is 33% (Phan et al., 2014), much larger than the electron thermal energy gain as of 4.3% (Phan et al., 2013). In magnetotail observations by the Cluster spacecraft, statistically, the ion enthalpy flux is the dominant outgoing energy flux, followed by comparable ion bulk flow flux and electron enthalpy flux (Eastwood et al., 2013); in a few diffusion region crossing events close to the X-line, the electron enthalpy flux is comparable to the ion enthalpy flux (Tyler et al., 2016). In a laboratory experiment for a region about two ion inertial lengths (d_i) surrounding the X-line (within the ion diffusion region [IDR]), it was found that the ion-to-electron energy gain ratio is about 2 for symmetric reconnection (Yamada et al., 2014) and reduced to ~1.2 (31% for ions and 25% for electrons) for asymmetric reconnection (Yoo et al., 2017). A particle-in-cell (PIC) simulation of symmetric reconnection shows that integrating over the entire simulation domain, the ion and electron energy gains are 25 and 15% of the input field energies, respectively, with a ratio of ~1.6 (Li et al.,

2015). These studies suggest a general trend that ions gain more energy than electrons during reconnection, while the energy partition may depend on the distance from the X-line. In this study, we will analyze such dependence.

During reconnection with a guide field, the Poynting flux from the guide field is considered to be largely redirected from the inflow to the outflow directions without being transferred to kinetic energy fluxes of plasmas, for example, based on the magnetohydrodynamic (Birn & Hesse, 2010) and PIC simulation studies (Birn & Hesse, 2010; Lu et al., 2013). A simulation study of relativistic pair plasma symmetric reconnection suggests that as the guide field increases from 0 to 2 times of the reconnecting magnetic field, both the reconnection rate and the energy conversion from field to plasma energies are reduced, due to decrease of the compressibility (Werner & Uzdensky, 2017). For nonrelativistic proton-electron symmetric reconnection simulations, as the guide field increases from zero to a strength comparable to the reconnecting magnetic field, the electron thermal energy gain is greater than the electron bulk flow energy gain, while the ratio between the two decreases (Lu et al., 2013). With a guide field comparable to the reconnecting magnetic field, the perpendicular electron heating tends to be suppressed (Shay et al., 2014). Consistent with the Shay et al. (2014) study, Guo et al. (2017) found that the ratio between the electron parallel and perpendicular energies (for both flow and thermal energies) increases with the increasing guide field strength from 0 to 3 times of the reconnecting component. The guide field effect on the energy partition for proton-electron reconnection with asymmetric upstream conditions has not been addressed. In this study, we will discuss this question using PIC simulations.

An immediately relevant question to energy partition is how the energy is converted to energize particles. When plasmas are mostly frozen-in, the particle motion is organized by the magnetic field, and the energy conversion may be discussed in terms of the relative importance of the electric fields parallel ($E_{//}$) and perpendicular ($E_\perp$) to the magnetic field, which is typically used for discussing electron energization. For symmetric reconnection with negligible guide field, PIC simulation studies showed that for electrons in the entire simulation domain, $E_{//}$ and $E_\perp$ are more important for energizing low- and high-energy populations, respectively (Dahlin et al., 2014). Integrating over all energies, $E_\perp$ dominates the electron energization, particularly through Fermi-type acceleration due to the curvature drift (Dahlin et al., 2014; Li et al., 2015; Wang et al., 2016, 2017). The large-scale $E_{//}$ helps trap electrons in the reconnection exhaust, enabling the electrons to experience continuous Fermi acceleration, and influences the energy partition between ions and electrons (Haggerty et al., 2015). With increasing guide fields, $E_{//}$ becomes more important for electron energy gain, compared to the Fermi mechanism (Dahlin et al., 2015, 2016; Wang et al., 2016, 2017), and the most efficient acceleration occurs in the vicinity of the X-line (Fu et al., 2006; Huang et al., 2010).

In the diffusion region, where the particle motion cannot be described with the guiding center approximation, one instructional aspect to discuss about the energy conversion is the relative importance of the reconnection electric field (E_r) and the in-plane electric field (E_{xz}). For ions, both E_r and E_{xz} have been shown to contribute to energization by magnetotail observations (e.g., Nagai et al., 2015). Laboratory experiments (Yoo et al., 2014, 2017) and a simulation study (Liu et al., 2015) suggested that E_{xz} is quantitatively more important for the energization of protons. For electrons during symmetric reconnection, significant energization occurs in the central diffusion region mainly contributed by E_r (Shuster et al., 2015; Yamada et al., 2014, 2016; Zenitani et al., 2011), while E_{xz} does negative work inside the electron outflow jet (e.g., Karimabadi et al., 2007). A recent PIC simulation study of asymmetric reconnection suggests the dominant role of E_{xz} in energizing magnetosheath (high-density) electrons on the magnetospheric (low-density) side electron diffusion region (EDR; Swisdak et al., 2018). Cassak et al. (2017) further showed that adding a guide field, E_r gradually becomes more important than E_{xz} for the EDR electron energization. We will assess the contribution from E_r and E_{xz} on electron and ion energization in the asymmetric reconnection diffusion region in this study to obtain further understanding.

In this study, we will use PIC simulations to analyze the energy partition and conversion during asymmetric reconnection in the diffusion region and show one example observation event from Magnetosphere Multiscale (MMS) mission for the energy partition analysis. Section 2 will introduce the simulation and observation data we use and the basic equations for the energy partition analysis. The simulation results will be shown in section 3. The observation results will be shown in section 4. Conclusions and further discussions are in section 5.

2. Simulation Data and Energy Conversion Formulation

2.1. Simulation Data

The two-dimensional (2-D) PIC simulations use the VPIC code (Bowers et al., 2008). The coordinate is defined with x along the upstream reconnecting component of the magnetic field on the magnetospheric side, z is normal to the current sheet pointing toward the magnetosphere, and y is out of the reconnection plane to complete the right-handed orthogonal xyz coordinate. The simulation starts with an ion-scale Harris current sheet with a sinusoidal perturbation in B_z. Profiles of the magnetic field, density, and temperature are set up to maintain the pressure balance between the magnetospheric and the magnetosheath sides. Between the magnetosheath and the magneospheric upstream, the ratio of B_x is 1/1.37, the density ratio is 8, and the temperature ratio is 1. Other parameters are as follows: ratio of the upstream magnetosheath electron plasma and cyclotron frequencies $\omega_{pe}/\omega_{ce} = 2$, mass ratio $m_i/m_e = 100$, and temperature ratio $T_i/T_e = 2$. The simulation domain has $75 \times 25\ d_i$ resolved by $3{,}072 \times 2{,}048$ cells, with an average of 6,000 particles per cell, where d_i is the ion inertial length in the magnetosheath. The total energy in the simulations is well conserved, with an increase within 0.1% throughout the simulation time of 80 ω_{ci}^{-1}. The x direction has periodic boundary conditions, and the z direction boundary condition is reflecting for particles and conducting for fields. In this study, we present data from three simulation runs. One has zero guide field, and the other two have constant guide fields (B_g) pointing along the positive y direction (same as the reconnection current direction) in the entire domain. The guide field strengths are 0.2 and 1 times the reconnecting component of the magnetic field in the upstream magnetosheath (B_0).

The reconnection rate development of the three runs does not have significant differences, all rising to a peak of ~0.11 to 0.13 $V_A B_0$ around 60 ω_{ci}^{-1} and going to a steady state with a slight decrease (not shown), where V_A is the ion Alfvén speed based on B_0 and the magnetosheath density and ω_{ci} is the magnetosheath ion cyclotron frequency. To study the guide field effect on energy conversion, we select the time steps for the three runs with the same reconnection rate of 0.11 $V_A B_0$. For $B_g = 0$, 0.2, and 1, the selected time steps are 64, 78, and 62 ω_{ci}^{-1}, respectively.

In the following discussions, all quantities are shown in normalized units. Lengths are in unit of d_i, magnetic fields in B_0, density in the magnetosheath value (n_0), velocities in V_A, electric fields in $V_A B_0$, temperature in $m_e V_A{}^2$, and time in ω_{ci}^{-1}.

2.2. Observation Data

The observation data are from MMS (Burch et al., 2015). Ion and electron measurements are from burst-mode Fast Plasmas Investigation (FPI; Pollock et al., 2016), with the time resolution of 0.15 s for ions and 0.03 s for electrons. Magnetic field data are from the burst-mode Flux Gate Magnetometer (FGM; Russell et al., 2016) with a resolution of 128 samples per second.

2.3. Energy Conversion Formulation

The energy conversion is governed by the Poynting theorem (Birn & Hesse, 2005):

$$\frac{\partial}{\partial t}\left(\frac{\varepsilon_0 E^2}{2} + \frac{B^2}{2\mu_0}\right) + \nabla \cdot \mathbf{S} = -\mathbf{J}\cdot\mathbf{E} \tag{1}$$

where $\mathbf{S} = \mathbf{E} \times \mathbf{B}/\mu_0$ is the Poynting flux. $\mathbf{J} \cdot \mathbf{E}$ represents the energy conversion rate from electromagnetic fields to plasmas. The transport equation describes the plasmas energy gain in specific energy forms, which for the two-fluid dynamics is written as (Yamada et al., 2016)

$$\frac{\partial}{\partial t}\left[\frac{\varepsilon_0 E^2}{2} + \frac{B^2}{2\mu_0} + \sum_{s=e,i}\left(u_s + \frac{\rho_s}{2}V_s^2\right)\right] + \nabla\cdot\left[\mathbf{S} + \sum_{s=e,i}(\mathbf{K}_s + \mathbf{H}_s + \mathbf{q}_s)\right] = 0 \tag{2}$$

where u_s is the internal energy of species s defined as $u_s = Tr(\mathbf{P}_s)/2$, $\mathbf{P}_s$ is the pressure tensor, ρ_s is the mass density, V_s is the bulk speed, $\mathbf{K}_s = (\rho_s/2)V^2\mathbf{V}$ is the flow energy flux, $\mathbf{H}_s = u_s\mathbf{V}_s + \mathbf{P}_s \cdot \mathbf{V}_s$ is the enthalpy flux, and $\mathbf{q}_s$ is the heat flux vector ($\mathbf{q}_{s,\,j} = (Q_{s,\,jjj} + Q_{s,\,jkk} + Q_{s,\,jmm})/3$), where j, k, and m represent x, y, and z components and the heat flux tensor is defined as $\mathbf{Q}_s = \int m_s(\mathbf{v} - \mathbf{V}_s)(\mathbf{v} - \mathbf{V}_s)(\mathbf{v} - \mathbf{V}_s)f d^3v$. For a 2-D system, integrating equation (2) over an arbitrary rectangular region with a length along x of D and a width along z of δ leads to
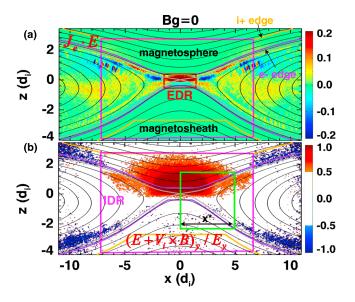
Figure 1. Illustration of regions for the energy partition analysis. Color-coded quantities are (a) rate of electron energy gain from the electric field ($J_e \cdot E$) and (b) normalized y component of the electric field in the ion rest frame $(E + V_i \times B)_y / E_y$. The red box marks the boundaries of the electron diffusion region (EDR) defined by enhanced $J_e \cdot E$, and the magenta box marks the boundaries of the ion diffusion region (IDR) defined by enhanced $(E + V_i \times B)_y / E_y$. The grey curves mark the magnetic separatrices. The pair of purple (orange) curves marks z locations of electron (ion) edges. See text for more details about the edge definition. The green box in (b) shows an example region for the electron-edge analysis: The x range is between the X-line and a variable x location $x = x^*$, and the z range is between the electron edges at x^*.

$$\int_{xl}^{xr}(S_z(x,z1) - S_z(x,z2))dx - \int_{z1}^{z2}\int_{xl}^{xr}\frac{\partial}{\partial t}\left(\frac{\varepsilon_0 E^2}{2} + \frac{B^2}{2\mu_0}\right)dxdz =$$

$$\int_{z1}^{z2}(S_x(xr,z) - S_x(xl,z))dz + \Delta U_{Ki} + \Delta U_{thi} + \Delta U_{Ke} + \Delta U_{the} \quad (3)$$

$$+ \int_{z1}^{z2}\int_{xl}^{xr}\nabla\cdot(\mathbf{q}_i + \mathbf{q}_e)dxdz$$

where Gauss' theorem is used to turn the volume integral into surface integral. The double-integral symbol hereafter represents the 2-D integral over the selected region, the integral over x is taken at the inflow boundaries between the x boundaries of the selected region (xl and xr; l and r represent the left and right boundaries, respectively, and $xr = xl + D$), and the integral over z is taken at the outflow boundaries between the z boundaries of the selected region ($z1$ and $z2$, $z2 = z1 + \delta$). Here $S_z(x,z1)$ and $S_z(x, z2)$ represent the z component of the Poynting flux at the magnetosheath and magnetospheric inflow boundaries, respectively ($z = z1$ and $z = z2$). As discussed in Birn and Hesse (2010), the Poynting flux due to the guide field is largely redirected without being converted to particle's energy flux, which is confirmed with our simulations. Thus, for the energy partition analysis, we only include the contribution by the reconnecting component of the magnetic field. Thus, we define $S_{in1} = -\left(\int_{xl}^{xr}E_y(x,z1)B_x(x,z1)dx\right)/\mu_0 D$ and $S_{in2} = \left(\int_{xl}^{xr}E_y(x,z2)B_x(x,z2)dx\right)/\mu_0 D$ as the local inflowing Poynting flux from the magnetosheath and magnetospheric sides, respectively, both with positive signs for pointing into the selected region. Along with the temporal change of the magnetic field energy inside the selected region, we define the input field energy available for conversion as $U_{in} = (S_{in1} + S_{in2})D - \iint \frac{\partial}{\partial t}\left(\frac{\varepsilon_0 E^2}{2} + \frac{B^2}{2\mu_0}\right)dxdz$.

Terms on the right-hand side of equation (3) represent how energies are repartitioned during reconnection. The first term represents the outgoing magnetic field energy, where $S_x(xl,z)$ and $S_x(xr,z)$ are taken at the left and right boundaries of the selected region, respectively. The change of the bulk flow energy is

$$\Delta U_{Ks} = \int_{z1}^{z2}(K_{sx}(xr,z) - K_{sx}(xl,z))dz - \int_{xl}^{xr}(K_{sz}(x,z1) - K_{sz}(x,z2))dx + \iint\frac{\partial}{\partial t}\left(\frac{\rho_s}{2}V_s^2\right)dxdz \quad (4)$$

The change of the thermal energy is

$$\Delta U_{ths} = \int_{z1}^{z2}(H_{sx}(xr,z) - H_{sx}(xl,z))dz - \int_{xl}^{xr}(H_{sz}(x,z1) - H_{sz}(x,z2))dx + \iint\frac{\partial}{\partial t}(u_s)dxdz \quad (5)$$

The last term in equation (3) represents the change of the heat flux. The energy gain for species s is $\Delta U_s = \iint \mathbf{J}_s \cdot \mathbf{E}dxdz = \Delta U_{Ks} + \Delta U_{ths} + \iint\nabla\cdot\mathbf{q}_s dxdz$, where $\mathbf{J}_i = ne\mathbf{V}_i$ and $\mathbf{J}_e = -ne\mathbf{V}_e$, n is the number density, e is the unit charge, and $V_{i(e)}$ is the ion (electron) bulk velocity. The rate of the energy gain relative to the input field energy is $\iint\mathbf{J}_s \cdot \mathbf{E}dxdz/U_{in}$, and the difference between $\iint(\mathbf{J}_i \cdot \mathbf{E} + \mathbf{J}_e \cdot \mathbf{E})dxdz/U_{in}$ and unity represents the rate of energy that is carried away by the outgoing Poynting flux.

3. Simulation Results

3.1. Energy Partition

Figure 1 illustrates the regions for the energy partition analysis. The profile of $J_e \cdot E$ for $B_g = 0$ (Figure 1a), the electron energy gain from the electric field per unit volume and per unit time, is most enhanced close to the X-line ($[x, z] = [0, 0]$). The pair of purple curves marks the selected electron edges, that is, z boundaries of meandering or exhaust electrons, which will be used as the z boundaries for the energy partition analysis. At $x = 0$, the positive $J_e \cdot E$ region extends to $z = 0.4$ d_i on the magnetospheric side, which is defined as the electron edge close to the X-line ($z_{e,x}$). In the EDR with weak guide field, demagnetized electrons perform meandering motion across the current layer. We define the electron edge on the magnetosheath side so that the z-distance from the X-line (z_{sh}) is the same as that on the magnetospheric side, that is, $|z_{sh}| = |z_{e,X}|$. We

have confirmed with electron distributions that the above defined boundaries based on $\mathbf{J_e} \cdot \mathbf{E}$ well represent the edges for meandering electrons in the EDR. As $|x|$ increases, the exhaust region becomes broader in z. We define that at a certain x, for each of the magnetospheric and magnetosheath side, the larger quantity of $|z_{spx}| + 0.2 \, d_i$ and $|z_{e,x}|$ is selected as the electron edge, where $|z_{spx}|$ is the distance between the magnetic separatrix on the same side and $z = 0$. Using $|z_{spx}| + 0.2 \, d_i$ instead of $|z_{spx}|$ is to ensure enclosing all electrons in the exhaust, taking into account the finite gyroradius effect. For the energy partition analysis, we have confirmed that the conclusion is insensitive to the choice of the z boundary in the range of $|z_{spx}|$ to $|z_{spx}| + 0.3 \, d_i$. Along the x direction, the major $\mathbf{J_e} \cdot \mathbf{E} > 0$ region extends to $x \sim 1.5 \, d_i$ before it switches to large negative values for $z > 0$. The x locations of the $\mathbf{J_e} \cdot \mathbf{E}$ sign reversal, together with their corresponding z locations of electron edges, are defined as the boundaries of the EDR (marked by the red rectangular) in this study. We note that close to the X-line, because the current is mainly carried by electrons, $\mathbf{J_e} \cdot \mathbf{E}$ is almost identical to $\mathbf{J} \cdot \mathbf{E}' = \mathbf{J} \cdot (\mathbf{E} + \mathbf{V}_e \times \mathbf{B})$, where the positive $\mathbf{J} \cdot \mathbf{E}'$ has been shown to be a good indicator for the central EDR with nonideal energy dissipation (Zenitani et al., 2011).

Figure 1b shows the profile of the y component of the nonideal electric field normalized by E_y $((E + V_i \times B)_y/E_y)$. Large values with amplitudes greater than 0.5 mean that the nonideal component contributes more than 50% of E_y, indicating significant ion demagnetization (e.g., Aunai et al., 2011a). Regions with absolute values lower than 0.5 are colored in white. At $x = 0$ on the magnetospheric side, $(E + V_i \times B)_y/E_y$ drops to 0.5 at $z_{i,x} = 2.7 \, d_i$. Analogous to the electron edge definitions, z locations with the maximum between $|z_{i,x}|$ and $|z_{spx}| + 1 \, d_i$ are selected as the ion edges, marked as the orange pair of curves in Figure 1. The x locations where $(E + V_i \times B)/E_y$ drops to 0.5, along with their corresponding z locations of the ion edges, are considered as boundaries of the IDR (marked by magenta boxes) in this study.

For each simulation run, two sets of the energy partition analyses are performed, with z boundaries defined by the electron and ion edges, respectively. For each set of the analysis, one x boundary is fixed at the X-line, while the other boundary, at a downstream distance denoted by x^*, is left as a parameter that we vary to determine how the energy budget changes with downstream distance from the X-line. The green box in Figure 1b shows an example region for the electron-edge analysis at $x^* = 5$. When the guide field is finite, the two sides of the exhausts are not symmetric. The sign of x^* is defined to be positive in $x > 0$ where the Hall magnetic field in the exhaust has the opposite sign with B_g. With the above definitions, ion and electron edges for different runs are individually defined and do not have identical z values.

The energy partition analysis results as functions of x^* and B_g are shown in Figure 2. Between electron edges, at $|x^*|$ smaller than the end of the EDR (marked by diamonds on each curve), the energy deposition rate to electrons ($\Delta U_e/U_{in}$) is large (Figure 2a). By the end of the EDR, $\Delta U_e/U_{in}$ decreases from 70 to 90% for $B_g \leq 0.2$ to about 50% for $B_g = 1$. In contrast, the energy deposition rate to ions ($\Delta U_i/U_{in}$; Figure 2b) is small, around -10 to 10% with a slight increase with B_g. As will be discussed in section 3.3, the electric field does negative work to ions in the EDR mainly due to the deceleration by E_z for magnetosheath ions. We conclude that at the EDR scale, electrons gain most of the converted electromagnetic energies; the fraction of input electromagnetic energy that is converted to plasmas $((\Delta U_i + \Delta U_e)/U_{in})$ decreases from $B_g = 0$ to $B_g = 1$. Very close to the X-line, for example, within 1 d_i for $B_g = 0$, $(\Delta U_i + \Delta U_e)/U_{in}$ is greater than unity. It is because U_{in} is defined as the input electromagnetic energy only from the inflow boundary. Close to the X-line, the x component of the Poynting flux contributed by $E_z < 0$ and Hall B_y near the current sheet midplane points toward $x = 0$, a feature specific for asymmetric reconnection that is discussed in Swisdak et al. (2018). According to the formulation, such inward Poynting flux contributes additional electromagnetic energy from the outflow boundary to the EDR. Since the input electromagnetic energy U_{in} decreases with the decreasing size of the analysis region, the energy partition normalized by U_{in} for small x^* has large uncertainty. Therefore, quantities normalized by U_{in} are only shown for $|x^*| > 0.5$, where the integral of the two sides of equation (1) are well balanced, with their difference within 5% of the input energy U_{in}.

The rate of the ion energy gain becomes greater than the rate of the electron energy gain at the IDR scale. Figures 2c and 2d show the results of energy partition analysis between ion edges. The rate of the electron energy gain (Figure 2c) decreases with increasing $|x^*|$. Near the end of the IDR (marked by circles), $\Delta U_e/U_{in}$ averaged between the two exhausts approaches to roughly a constant of 20%, while with finite B_g, asymmetry exists between the two sides (higher for $x^* > 0$). $\Delta U_i/U_{in}$ (Figure 2d) increases with increasing $|x^*|$, which
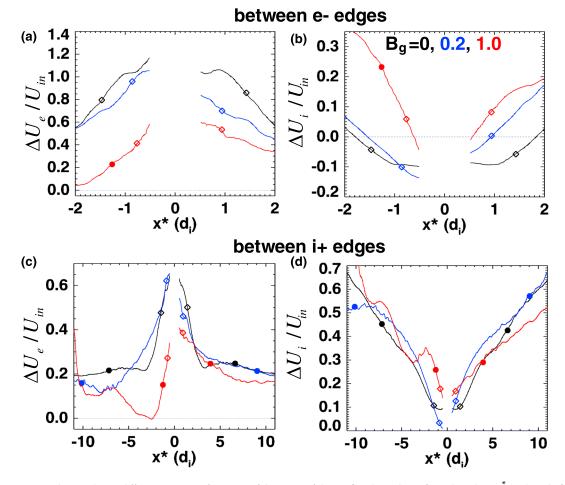
Figure 2. Energy partition in the simulation diffusion region as functions of distances of the outflow boundaries from the X-line (x^*) and guide field strength ($|B_g|$). (a and c) Energy deposition rate to electrons (). (b and d) Energy deposition rate to ions ($\Delta U_i/U_{in} = \iint \mathbf{J}_i \cdot \mathbf{E}\,dx\,dz/U_{in}$). Panels (a) and (b) are analyses with z ranges between electron edges; panels (c) and (d) are analyses with z ranges between ion edges. Different colors represent different B_g: the black, blue, and red are for $B_g = 0$, 0.2, and 1, respectively. Diamonds on curves mark the x locations of the end of the electron diffusion region (EDR), and circles mark the end of the ion diffusion region (IDR). From EDR to IDR scales, the energy partition changes from $\Delta U_e > \Delta U_i$ to $\Delta U_e < \Delta U_i$. With finite B_g, in the EDR, the electron energy gain is reduced; at the IDR scale, the overall rates of ion and electron energy gains are not much affected but exhibit asymmetry between the two exhausts.

reaches about 30 to 60% by the end of the IDR and further increases downstream of the IDR. With the IDR definition we use in the present study, the end of the IDR is closer to the X-line for $B_g = 1$ than for $B_g = 0$. $\Delta U_i/U_{in}$ is smaller at the $|x^*|$ of the IDR end, while $\Delta U_i/U_{in}$ at the same $|x^*|$ locations does not differ much. The finite guide field also creates an asymmetry in $\Delta U_i/U_{in}$ between the two exhausts, higher at $x^* < 0$ (opposite to the effect for electrons). We have also confirmed that U_{in} is almost independent of B_g, such that the above-mentioned guide field effects also hold if we compare the energy gain without being normalized by U_{in}.

Past studies have shown that during asymmetric reconnection with guide fields, the electron diamagnetic drift close to the X-line leads to the motion of the X-line and asymmetries in the plasma flow, exhaust opening angles, etc., between the two exhausts (e.g., Pritchett & Mozer, 2009; Swisdak et al., 2003). Here the asymmetry between the two exhausts is revealed from the aspect of the ion and electron energy gains. We note that the X-line motion in the simulation is negligible, and all presented results based on the quantities in the simulation frame are essentially the same as the results in the X-line frame.

Close to the end of the EDR, the rate of the electron energy gain is smaller for the ion-edge analysis (Figure 2c) than that for the electron-edge analysis (Figure 2a). The rate of the ion energy gain is larger for the ion-edge analysis (Figure 2d) than that for the electron-edge analysis (Figure 2b) but is much smaller than the rate of the electron energy gain in both analyses. In short, the smaller the region size is, the more dominant the rate
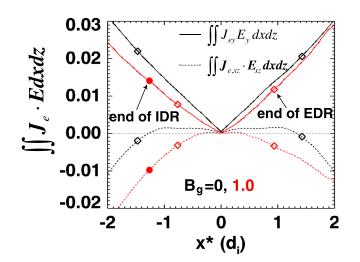
Figure 3. Electron energy gain decomposed into the work done by the reconnection electric field E_y ($\iint J_{ey}E_y dxdz$, solid curves) and that by in-plane electric fields ($\iint \mathbf{J}_{e,xz} \cdot \mathbf{E}_{xz} dxdz$, dashed curves) for $B_g = 0$ and $B_g = 1$. Electron edges are used as z boundaries of integration regions. Colors represent $|B_g|$, diamonds mark the end of the electron diffusion region (EDR), and circles mark the end of the ion diffusion region (IDR). The positive electron energy gain dominantly comes from E_y. In-plane electric fields have a finite positive contribution close to the X-line, which is reduced at strong $|B_g| = 1$, compared to $|B_g| = 0$.

of the electron energy gain is. From the EDR to the IDR scales, the energy partition changes from $\Delta U_e > \Delta U_i$ to $\Delta U_e < \Delta U_i$.

3.2. Electron Energy Conversion

In this section, we analyze which components of the electric fields contribute to electron energization close to the EDR.

Figure 3 shows the integral of $\mathbf{J}_e \cdot \mathbf{E}$ over the analysis regions using electron edges as z boundaries for $B_g = 0$ and $B_g = 1$ (without normalizing by U_{in}). $\mathbf{J}_e \cdot \mathbf{E}$ is decomposed into the contribution by the reconnection electric field $W_{e,y} = \iint J_{ey}E_y dxdz$ (solid curves) and by in-plane electric fields $W_{e,xz} = \iint (J_{ex}E_x + J_{ez}E_z) dxdz \equiv \iint \mathbf{J}_{e,xz} \cdot \mathbf{E}_{xz} dxdz$ (dashed curves). For all guide field cases (including $B_g = 0.2$ that is not shown), the major positive contribution comes from E_y; in-plane electric fields have a small positive contribution close to the X-line and a negative contribution at the larger x locations. The electron energization in terms of the 2-D profiles of $\mathbf{J}_e \cdot \mathbf{E}$ in asymmetric reconnection simulations was discussed in previous studies (e.g., Pritchett & Mozer, 2009; Swisdak et al., 2018; Cassak et al., 2017). We will discuss the similarities and differences between the results presented here and in these earlier studies in section 5.

With a guide field of 1, $W_{e,y}$ has a decrease compared to the case with zero guide field (Figure 3). The total $W_{e,y}$ in the entire EDR (at the points marked by diamonds) for $B_g = 1$ is 50% of that for $B_g = 0$. $W_{e,y}$ integrated over the same x range is also reduced from $B_g = 0$ to $B_g = 1$. Using the x range of the EDR for $B_g = 0$ ($|x^*| \sim 1.5$), the average $W_{e,y}$ between two sides of the exhaust for $B_g = 1$ is 84% of that for $B_g = 0$. Figures 4a and 4b show 2-D profiles of $J_{ey}E_y$ for the two runs, and Figure 4e shows the 1-D cuts of $J_{ey}E_y$ across $x = 0$. The clearest change as adding a strong guide field is that the current layer, that is, the $J_{ey}E_y$ enhanced region, becomes narrower in z, which causes the decrease in $W_{e,y}$. Qualitatively speaking, since the upstream temperature is not negligible, the electron current layer thickness should be on the order of the electron thermal gyroradius based on the average magnetic field strength in the current layer. The guide field makes the magnetic field strength stronger in the current layer, and hence, the thickness becomes smaller than the $B_g = 0$ case (Hesse et al., 2013). Since the Hall magnetic field in the exhaust is opposite to the guide field in $x^* > 0$ and is along the guide field direction in $x^* < 0$, the increase of the magnetic field strength and the decrease of the current layer thickness by the guide field are smaller in $x^* > 0$ than in $x^* < 0$. The asymmetries of B_y and the current layer thickness between two sides of the exhausts likely cause asymmetry in $W_{e,y}$ between the two sides ($x^* < 0$ and $x^* > 0$; Figure 3).

For $W_{e,xz}$ (dashed curves in Figure 3), the positive contribution close to the X-line is clearly decreased from $B_g = 0$ to $B_g = 1$. Figures 4c and 4d show the profiles of $\mathbf{J}_{e,xz} \cdot \mathbf{E}_{xz}$, and Figure 4f shows the 1-D cuts of $\mathbf{J}_{e,xz} \cdot \mathbf{E}_{xz}$ across $x = 0$. Positive values occur close to the X-line; at x distances near the end of the central EDR and further downstream, $\mathbf{J}_{e,xz} \cdot \mathbf{E}_{xz}$ becomes mostly negative.

Let us start with $B_g = 0$. As discussed in previous studies, the in-plane electric potential is set up due to the decoupling between ions and electrons (e.g., Fujimoto, 2014). Overall, electrons are easier to be carried by magnetic fields into the current sheet and accelerated away from the X-line toward downstream, such that the Hall E_z points from the inflow toward the current sheet, and E_x points away from the X-line (e.g., Fu et al., 2006; Fujimoto, 2014). Close to the X-line for asymmetric reconnection, the in-plane electric field (dominant by Hall $E_z < 0$) is set up mainly to maintain the charge neutrality at the sharp pressure gradient from the magnetosheath to the magnetosphere (e.g., Willis, 1971; Pritchett, 2008; Burch et al., 2016). Consequently, a strong $\mathbf{J}_{e,xz} \cdot \mathbf{E}_{xz} > 0$ region exists where $V_{ez} > 0$: between the magnetospheric side stagnation point ($V_{ez} = 0$) and the z location slightly on the magnetosheath side of the X-line (Figure 4c). The $\mathbf{J}_{e,xz} \cdot \mathbf{E}_{xz} < 0$ region further on the magnetosheath side corresponds to where $E_z > 0$, that is, the magnetosheath side counterpart of the Hall field. Further downstream than about the end of the central EDR (marked by vertical dashed lines), electrons have large bulk velocities and leave ions
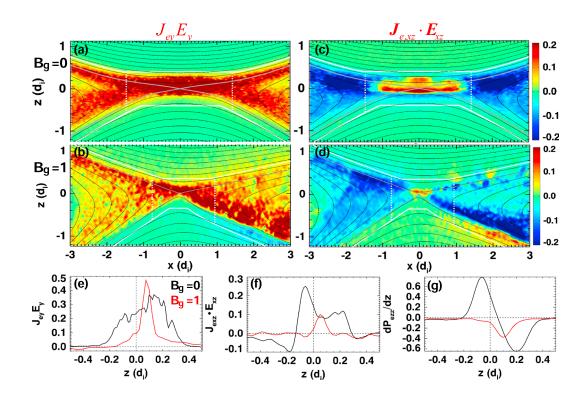
Figure 4. (a and b) 2-D profiles of $J_{ey}E_y$ for $B_g = 0$ and $B_g = 1$; (c and d) 2-D profiles of $\mathbf{J}_{e,\,xz} \cdot \mathbf{E}_{xz}$ for $B_g = 0$ and $B_g = 1$. The solid white curves mark z locations of electron edges. (e–g) 1-D cuts of $J_{ey}E_y$, $\mathbf{J}_{e,\,xz} \cdot \mathbf{E}_{xz}$, and dP_{ezz}/dz across $x = 0$ for $B_g = 0$ (black) and $B_g = 1$ (red). Adding a guide field, the electron current layer becomes narrower along z, which leads to a decrease in the total energy conversion by E_y in the electron diffusion region. $\mathbf{J}_{e,\,xz} \cdot \mathbf{E}_{xz}$ provides a positive electron energy gain near the X-line and does negative work on electrons around the end of the electron diffusion region (marked by white dashed lines) and beyond. The positive contribution decreases with increasing guide field strength. The reduced $\mathbf{J}_{e,\,xz} \cdot \mathbf{E}_{xz}$ is associated with the lack of positive dP_{ezz}/dz close to the X-line for $B_g = 1$ (g). See text for more details.

behind. The in-plane electric fields are to hold back electrons and allow ions to catch up. Therefore, $\mathbf{J}_{e,\,xz} \cdot \mathbf{E}_{xz}$ is mostly negative.

With finite guide fields, the overall feature of $\mathbf{J}_{e,\,xz} \cdot \mathbf{E}_{xz}$ is the same: positive near the X-line and negative at large distances from the X-line (Figure 4d). For $B_g \leq 0.2$, the $\mathbf{J}_{e,\,xz} \cdot \mathbf{E}_{xz}$ does not change considerably (not shown). For $B_g = 1$, the positive values of $\mathbf{J}_{e,\,xz} \cdot \mathbf{E}_{xz}$ are much smaller than those for $B_g = 0$. As shown in Figure 4f, the peak value of $\mathbf{J}_{e,\,xz} \cdot \mathbf{E}_{xz}$ cut at $x = 0$ decreases by about 50% from 0.25 for $B_g = 0$ to 0.12 for $B_g = 1$. In addition, the region with positive $\mathbf{J}_{e,\,xz} \cdot \mathbf{E}_{xz}$ becomes much smaller: the positive $\mathbf{J}_{e,\,xz} \cdot \mathbf{E}_{xz}$ region is only on the magnetospheric side of the X-line, and its z extension of the positive $\mathbf{J}_{e,\,xz} \cdot \mathbf{E}_{xz}$ near $x = 0$ is about 0.2 d_i, much smaller than the z extension of 0.4 d_i for $B_g = 0$.

Let us further discuss why with sufficiently large B_g the positive contribution of $\mathbf{J}_{e,\,xz} \cdot \mathbf{E}_{xz}$ close to the X-line is reduced. At the X-line, the electron flow velocity is nonzero since the stagnation location is on the magnetospheric side. For in-plane electric fields, the nonideal component $(\mathbf{E} + \mathbf{V_e} \times \mathbf{B})$ is mainly due to in-plane $\nabla \cdot \mathbf{P_e}$, where dP_{ezz}/dz is the dominant term (not shown). We can decompose the in-plane electric fields as $E_x \sim B_y V_{ez} - B_z V_{ey}$ and $E_z \sim B_x V_{ey} - B_y V_{ex} - dP_{ezz}/dz/(ne)$. Thus,

$$\mathbf{J}_{e,xz} \cdot \mathbf{E}_{xz} = J_{ex}E_x + J_{ez}E_z \sim neV_{ey}(B_z V_{ex} - B_x V_{ez}) + V_{ez}dP_{ezz}/dz \qquad (6)$$

Close to the X-line where B_x and B_z are near zero, $\mathbf{J}_{e,\,xz} \cdot \mathbf{E}_{xz}$ is contributed by the last term $V_{ez}dP_{ezz}/dz$. For $B_g = 0$, P_{ezz} increases toward the magnetospheric side $(dP_{ezz}/dz > 0)$ near the X-line before a further decrease $(dP_{ezz}/dz < 0)$ to the magnetospheric inflow region, as shown in Figure 4g in black, consistent with those shown in previous studies (e.g., Chen et al., 2016, 2016; Shay et al., 2016). Electron distributions for $B_g = 0$ at the X-line and in the magnetosheath side inflow region are shown in Figures 5a and 5b to assist
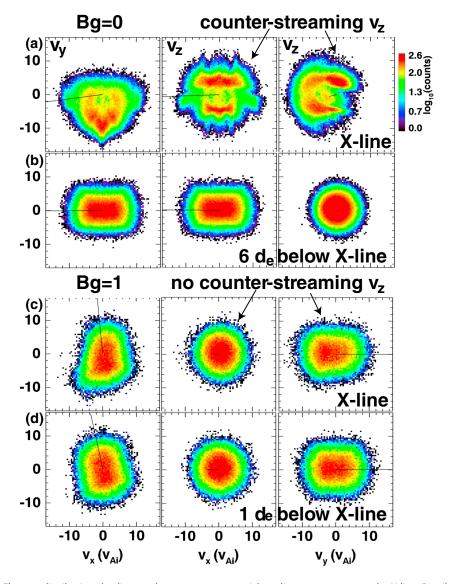
Figure 5. Electron distributions leading to electron pressure spatial gradient structures near the X-line. Distributions are taken at $x = 0$ from (a and b) $B_g = 0$ and (c and d) $B_g = 1$. Panels (a) and (c) are at the z locations of the X-line, while panels (b) and (d) are from the magnetosheath side of the X-line representing distributions in the electron inflow region. Three columns are for distributions in different velocity planes. The black lines in each panel indicate the magnetic field direction in the corresponding velocity plane. For $B_g = 0$, electrons bouncing multiple times in the electron diffusion region (with large negative v_y) are accumulated to increase the density, and they form counterstreaming v_z to increase T_{ezz}, both leading to a pressure increase compared to the inflow region. Such energized electrons with counterstreaming v_z and the pressure increase do not exist for $B_g = 1$.

understanding the P_{ezz} structure. The increase of P_{ezz} from the magnetosheath inflow region to the X-line is associated with the electron oscillatory meandering motion (e.g., Chen et al., 2011, 2016). Electrons with multiple bounces are accelerated by $E_y > 0$ during the meandering motion and thus appear with large negative v_y in the X-line distribution. When magnetosheath electrons move toward the magnetosphere, they are accelerated by $E_z < 0$ that extends to $z < 0$. Therefore, electrons in the distributions close to the X-line have considerable $|v_z|$. Electrons moving toward the magnetosphere and toward the magnetosheath together form counter streaming v_z (middle and right panels of Figure 5a) that leads to large $T_{ezz} (= P_{ezz}/n)$. Simulation data show that the density does not change much from the inflow to the X-line. Thus, the temperature enhancement leads to the P_{ezz} increase from the magnetosheath inflow region to the X-line vicinity. For the simulations with $B_g = 0.2$, we have confirmed that dP_{ezz}/dz is also positive
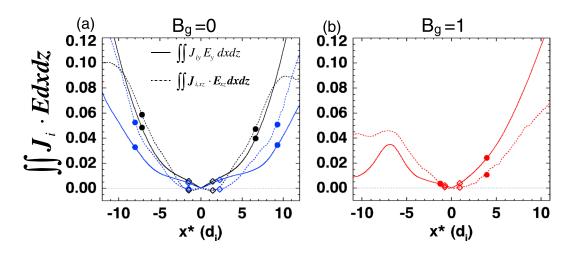
Figure 6. Ion energy gain decomposed into the work done by the reconnection electric field E_y ($\iint J_{iy}E_y dxdz$, solid curves) and that by in-plane electric fields ($\iint \mathbf{J}_{i,xz} \cdot \mathbf{E}_{xz} dxdz$, dashed curves). (a) $B_g = 0$; the black and blue curves are taken from $t\omega_{ci} = 64$ and $t\omega_{ci} = 72$, respectively. At the electron diffusion region scale, $\iint J_{iy}E_y dxdz$ dominates. At the ion diffusion region scale, at earlier time (close to the time for the peak reconnection rate), $\iint J_{iy}E_y dxdz$ and $\iint \mathbf{J}_{i,xz} \cdot \mathbf{E}_{xz} dxdz$ are comparable, while at later time, $\iint \mathbf{J}_{i,xz} \cdot \mathbf{E}_{xz} dxdz$ dominates. (b) $B_g = 1$; $\iint \mathbf{J}_{i,xz} \cdot \mathbf{E}_{xz} dxdz$ dominates at $x^* < 0$, while $\iint J_{iy}E_y dxdz$ dominates at $x^* > 0$ at all time.

near the X-line along with the existence of additional electrons to the inflowing component. Therefore, in the X-line vicinity, $\mathbf{J}_{e,xz} \cdot \mathbf{E}_{xz} \sim V_{ez} dP_{ezz}/dz$ is positive for weak B_g.

For $B_g = 1$, P_{ezz} monotonically decreases from the magnetosheath to the magnetospheric side ($dP_{ezz}/dz < 0$; red curve in Figure 4g). Thus, near the X-line, $\mathbf{J}_{e,xz} \cdot \mathbf{E}_{xz} \sim V_{ez} dP_{ezz}/dz$ is slightly negative for $B_g = 1$. The X-line distribution (Figure 5c) for $B_g = 1$, although nongyrotropic as discussed in Hesse et al. (2016), only exhibits acceleration toward $v_y < 0$ along the B_g without showing electrons with much larger $|v_z|$ than those in inflow distributions (Figure 5d). That is why P_{ezz} does not increase from the magnetosheath inflow to the X-line and is in fact slightly decreased.

On the magnetospheric side as z increases, dP_{ezz}/dz gradually becomes negative (for all B_g cases). dP_{ezz}/dz reversal occurs before reaching the electron stagnation location ($V_{ez} = 0$). Between the locations of dP_{ezz}/dz reversal and V_{ez} reversal, positive $\mathbf{J}_{e,xz} \cdot \mathbf{E}_{xz}$ comes from $-neV_{ey}B_xV_{ez}$ (second term in equation (6)) with $V_{ey} < 0$, $B_x > 0$, and $V_{ez} > 0$. We observe reduced distances between the X-line and the stagnation location, which causes the reduced extension of the positive $\mathbf{J}_{e,xz} \cdot \mathbf{E}_{xz}$ region, and hence the decrease of the net positive contribution of $\mathbf{J}_{e,xz} \cdot \mathbf{E}_{xz}$. The reduced distance between the X-line and the stagnation location was also shown with simulations with $B_g = 0.1$–4 in a recent study (Cassak et al., 2017), supported by their theory that this distance is proportional to the width of the diffusion region, which decreases with increasing B_g, because it scales with particles' thermal gyroradii.

3.3. Ion Energy Conversion in the Diffusion Region

The relative importance between in-plane and out-of-plane electric fields on ion energization is evaluated by integrating $\mathbf{J}_i \cdot \mathbf{E}$ by components, where ion edges are used as z boundaries. Results for $B_g = 0$ and $B_g = 1$ are shown in Figure 6. In each panel, solid curves are $W_{i,y} = \iint J_{iy}E_y dxdz$ and dashed curves are $W_{i,xz} = \iint (J_{ix}E_x + J_{iz}E_z)dxdz \equiv \iint \mathbf{J}_{i,xz} \cdot \mathbf{E}_{xz} dxdz$. For $B_g = 0$ (Figure 6a), we present the results at $t\omega_{ci} = 64$ with black curves (same time used in other plots for $B_g = 0$), which represent the situation close to the time at the peak reconnection rate ($t\omega_{ci} = 56$, not shown); in addition, the results at a later time $t\omega_{ci} = 72$ with a quasi-steady steady reconnection rate are shown with blue curves. For both the earlier and the later time, at the x locations around the EDR scale (x locations of the end of EDR are marked with diamonds), the energization by the reconnection electric field dominates over that by the in-plane electric fields. The contribution by the in-plane electric fields is in fact close to zero. The result at the IDR scale is time dependent: close to the time of the peak reconnection rate, $W_{i,y}$ and $W_{i,xz}$ are comparable; at the later time, the energization by the in-plane electric fields dominates. With $B_g = 1$ (Figure 6b), the most prominent feature is asymmetry between the two exhausts: in $x < 0$ (Hall magnetic field along the guide field direction), the contribution by the in-plane electric field dominates; in $x > 0$, the contribution by the reconnection electric field dominates.
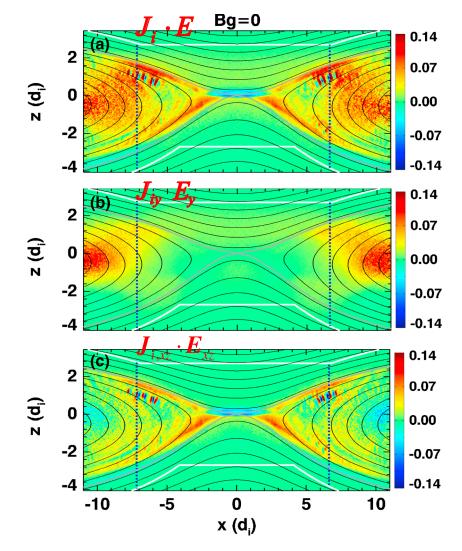
Figure 7. 2-D profiles of $\mathbf{J}_i \cdot \mathbf{E}$, $J_{iy}E_y$, and $\mathbf{J}_{i,\,xz} \cdot \mathbf{E}_{xz}$ for $B_g = 0$. The white solid curves mark the ion edges. The vertical blue dashed lines mark the x locations of the end of the ion diffusion region. E_y provides positive energization for ions at large z distances from the midplane. In-plane electron fields provide a negative contribution around the central electron diffusion region and positive contributions with larger values than E_y at large x distances.

Figure 7 shows 2-D profiles of $\mathbf{J}_i \cdot \mathbf{E}$, $J_{iy}E_y$, and $\mathbf{J}_{i,\,xz} \cdot \mathbf{E}_{xz}$ for $B_g = 0$. Within the IDR (boundaries marked by blue vertical lines), $J_{iy}E_y$ is enhanced at large $|z|$ locations away from the midplane, where the out-of-plane ion current is carried by meandering ions accelerated by E_y with finite gyroradius effects. We note that $J_{iy}E_y$ also has significant enhancements close to the front of the outward propagating reconnection structure ($\sim$8–10 d_i from the X-line), which is an important region for ion energization outside of the IDR, similar to the situation during symmetric reconnection (e.g., Lu et al., 2016; Sitnov et al., 2009). In-plane electric fields do negative work on ions around the central EDR where $E_z < 0$ and $V_{iz} > 0$. This is the same region where electrons gain energies from the in-plane electric fields (Figure 5). The role of E_z near the EDR in decelerating magnetosheath ions leading to negative $J_{iz}E_z$ was also shown in Pritchett (2008). The negative $J_{iz}E_z$ in the central EDR is a specific feature of asymmetric reconnection, where the stagnation location of ions is biased to the magnetospheric side of the X-line. At larger x distances from the X-line, $\mathbf{J}_{i,\,xz} \cdot \mathbf{E}_{xz}$ provides positive contributions with larger values than $J_{iy}E_y$, with the largest values close to the separatrices. Consequently, at small x locations, the positive ion energy gain mainly comes from E_y; at large x locations, in-plane electric fields become more important. As reconnection develops, in-plane electric fields further develop with increasing importance in energizing ions as shown in Figure 6a.
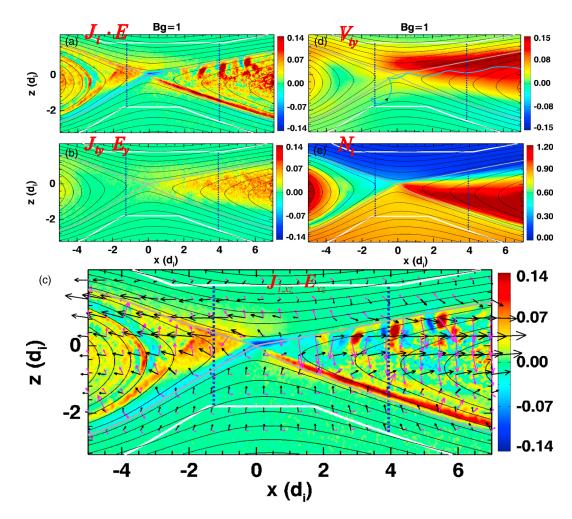
Figure 8. (a–c) 2-D profiles of $\mathbf{J}_i \cdot \mathbf{E}$, $J_{iy}E_y$, and $\mathbf{J}_{i,\,xz} \cdot \mathbf{E}_{xz}$ for $B_g = 1$. Formats are the same as in Figure 7. The black and magenta arrows in (c) show the in-plane ion flow and electric field vectors. The ion flow is toward $z > 0$ in both exhausts, while E_z has opposite signs, leading to stronger $\mathbf{J}_{i,\,xz} \cdot \mathbf{E}_{xz}$ in $x < 0$ than in $x > 0$. $J_{iy}E_y$ is stronger in $x > 0$ than in $x < 0$, understood with the bulk (d) V_{iy} and (e) density asymmetries. The light blue curve in (d) is an example ion trajectory. See texts for more details.

The asymmetric ion energization for $B_g = 1$ between the exhausts to the left and right of the X-line can be seen in 2-D $\mathbf{J}_i \cdot \mathbf{E}$ profiles (Figures 8a–8c). The asymmetric contribution by in-plane electric fields between the two exhausts is mainly due to the asymmetry in the z component of flow and electric field patterns. On top of the $\mathbf{J}_{i,\,xz} \cdot \mathbf{E}_{xz}$ profile (Figure 8c), the in-plane ion flow and electric field vectors are marked by the black and magenta arrows, respectively. E_z has opposite signs in the two exhausts (e.g., Hesse et al., 2017; Pritchett & Mozer, 2009), which can be seen from the magenta arrows in Figure 8c. The bulk V_{iz} is positive in both exhausts. Thus, $J_{iz}E_z$ is positive in $x < 0$ and negative in $x > 0$ for most of the exhaust region. Along with the positive $J_{ix}E_x$ due to V_{ix} and E_x away from the X-line, the integrated ion energy gain from in-plane electric fields is positive for both sides of the X-line but is greater in $x < 0$ than in $x > 0$ (Figure 6b).

The $\mathbf{J}_{i,\,xz} \cdot \mathbf{E}_{xz}$ pattern during asymmetric guide field reconnection has differences from that during symmetric guide field reconnection, mainly because of the change in flow patterns. Previous studies about symmetric guide field reconnection discussed that ions move across the magnetic field in the x-z plane, while electrons mainly move along the magnetic field within the ion-electron decoupling region (e.g., Kleva et al., 1995). Due to the acceleration by the parallel electric field, the net electron flow is toward $z > 0$ in $x < 0$ and toward $z < 0$ in $x > 0$. The ion bulk V_z is also positive in $x < 0$ and negative in $x > 0$ like electrons, to maintain the charge neutrality (e.g., Kleva et al., 1995; Pritchett & Coroniti, 2004). Because of the decoupling between the ion and electron motion, the charge neutrality is not perfectly maintained, which results in E_z with opposite signs in

the two sides of the exhaust (e.g., Pritchett & Coroniti, 2004), same as in asymmetric reconnection. The E_z in the exhaust has the same sign with $-V_{ix}B_y$ (e.g., Drake et al., 2009; Liu et al., 2014; Øieroset et al., 2016), and the Hall term also has a significant contribution (e.g., Fu et al., 2018).

To understand the asymmetric $J_{iy}E_y$ between two exhausts for guide field reconnection, we need to consider the ion flow along y, which is mostly parallel to the magnetic field. The ion flow outside of the diffusion region is dominant by the mostly magnetized magnetosheath populations. The flow can be roughly described as a field-aligned component pointing from the magnetosheath to the magnetospheric side, superposed on the convection with the magnetic field. In the $x > 0$ exhaust, the field line points from the magnetosheath to the magnetospheric side, and hence, the ion bulk velocity along the magnetic field is positive ($V_{i//} > 0$). Since the guide field $B_y > 0$, the y component of $V_{i//}$ is positive and is in the same direction with the reconnection electric field. Therefore, ions are accelerated by the reconnection electric field along the flow line. Similarly, in $x < 0$, $V_{i//}$ and V_{iy} are both negative. Ions that move from the magnetosheath toward the magnetosphere are decelerated by E_y. Therefore, the bulk V_{iy} (Figure 8d) and $J_{iy}E_y$ are largely positive in $x > 0$, while they are near-zero or slightly negative in the $x < 0$ exhaust.

Let us further discuss the asymmetric $J_{iy}E_y$ inside the diffusion region (between blue dashed lines). In the IDR, ions are demagnetized, so the description of a field-aligned motion plus convection with the magnetic field is not accurate. However, the flow pattern that the bulk V_{iy} is more positive in $x > 0$ than in $x < 0$ is still true (Figure 8d). In addition, the density is higher in $x > 0$ than in $x < 0$ (Figure 8e). E_y is mostly uniform throughout the IDR (not shown). The larger density and larger V_{iy} together lead to greater $J_{iy}E_y$ in $x > 0$ than in $x < 0$. The density and V_{iy} asymmetry can be further understood with the ion motion under the effect of E_x. In the magnetosheath inflow region, E_x is positive (seen from the rightward magenta arrows in Figure 8c). Magnetosheath ions that enter the $x < 0$ part of the diffusion region are moved toward the $x > 0$ side exhaust by the positive E_x, unless they initially have very large negative v_x. One example ion trajectory is shown with the light blue curve in Figure 8d. As such ions move in the diffusion region toward the positive x direction, they get accelerated by E_y. Consequently, the $x > 0$ side diffusion region contains more ions that have experienced much acceleration by E_y than the $x < 0$ side, resulting in a larger density and V_{iy}.

For the case with $B_g = 1$, the size of the IDR is reduced, as ions are more magnetized by the stronger magnetic field than those in reconnection with $B_g = 0$. In $x < 0$, the end of IDR occurs at $x \sim -1.3\ d_i$. A magnetic island is developed at $x < -3\ d_i$ (see the region with enhanced densities in $x < 0$ in Figure 8). We have a separate simulation with the same guide field strength (the number of particles per cell is doubled), where a magnetic island develops at a different location and the $x < 0$ side is an open exhaust. At the same reconnection phase, the IDR size in the separate simulation is about $2\ d_i$ in $x < 0$. We thus conclude that the reduced size of the IDR is insensitive to the existence of an island but is the result of the finite guide field. We have also confirmed that in the region outside of the magnetic island ($-2 < x^* < 0$), the energy partition conclusions and energization features discussed in this study are the same as the results in the open exhaust of the other simulation.

3.4. Test of the Observation Analysis Methods for Estimating Ion and Electron Thermal Energy Gain

In section 2, we obtained the formula to calculate the thermal energy gain (equation (5)). Normalizing it by the input magnetic energy U_{in} (defined in section 2) gives the rate of the field energy that is converted to the thermal energy:

$$dU_{th,s} = \frac{\int_{z1}^{z2}(H_{sx}(xr,z) - H_{sx}(xl,z))dz - \int_{xl}^{xr}(H_{sz}(x,z1) - H_{sz}(x,z2))dx + \iint \frac{\partial}{\partial t}(u_s)dxdz}{(S_{in1} + S_{in2})D - \iint \frac{\partial}{\partial t}\left(\frac{\varepsilon_0 E^2}{2} + \frac{B^2}{2\mu_0}\right)dxdz} \tag{7}$$

Equation (7) requires estimating the $\partial/\partial t$ terms and integrating over a certain region. In situ observations by the spacecraft only provide measurements for limited data points along the spacecraft trajectory. Thus, approximated formulas under certain assumptions are needed for applications to observation analysis. We follow the same derivation procedure as in Shay et al. (2014) but extract intermediate formulas with different amounts of assumptions. The formulas are for individual species, and we will drop the subscript s in variables.

At the magnetopause, typically the relative motion between the magnetopause and the spacecraft along the z direction leads to a crossing of the reconnection structure. Assume that the spacecraft makes such a
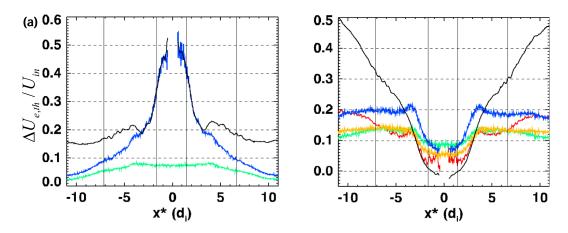
Figure 9. Tests of analysis methods for calculating the thermal energy gain ratio for $B_g = 0$. (a) Electron thermal energy gain ratio. (b) Ion thermal energy gain ratio. Black: exact calculation using equation (8); red: equation (11); blue: equation (12); orange: based on equation (12), changing the average temperature weighted by nV_x to that weighted by n; and green: equation (13). The blue curve in (a) and the red curve in (b) roughly agree with the black curves within a few d_i from the X-line and are applied to observations. The discrepancies at large distances are due to the invalid time-stationary assumption.

crossing along z at a fixed x location $x = D/2$. Let us analyze a region between $xl = -D/2$ and $xr = D/2$. When the guide field is sufficiently weak, the two sides of the exhausts are symmetric. Therefore, $\int_{z1}^{z2} (H_x(xr, z) - H_x(xl, z))dz = 2\int_{z1}^{z2} H_x(D/2, z)dz = 2\delta <H_x>$, where $<H_x>$ represents the average H_x at $x = D/2$ over $z1$ to $z2$. To make the analysis trackable, the quantities at the inflow boundaries are taken to be independent of x between $x = -D/2$ and $x = D/2$, such that the measurements of the inflow quantities at $x = D/2$ represent those along the entire inflow boundaries. We thus have $\int_{xl}^{xr}(H_z(x, z1) - H_z(x, z2))dx = D(H_{in1} + H_{in2})$, where $H_{in1} = H_z(D/2, z1)$ and $H_{in2} = -H_z(D/2, z2)$. Consequently, equation (7) evolves to

$$dU_{th} = \frac{2\delta <H_x> - D(H_{in1} + H_{in2}) + \iint \frac{\partial}{\partial t}(u_s)dxdz}{(S_{in1} + S_{in2})D - \iint \frac{\partial}{\partial t}\left(\frac{\varepsilon_0 E^2}{2} + \frac{B^2}{2\mu_0}\right)dxdz} \tag{8}$$

Next let us neglect $\partial/\partial t$ terms, which is valid within ~4 d_i from the X-line justified by our simulation analysis (Figure 9). Thus, according to the continuity equation of the mass density $\partial n/\partial t + \nabla \cdot (n\mathbf{V}) = 0$, the aspect ratio is estimated as

$$\frac{D}{\delta} = \frac{2 <nV_x>}{n_1 V_{in1} + n_2 V_{in2}} \tag{9}$$

where $n_{1,2}$ are the number densities at the two inflow boundaries, and $V_{in1,2}$ are inflow speeds. When the pressure tensor at the inflow boundary can be approximated by an isotropic pressure, the inflowing enthalpy flux becomes $H_{in1} = \frac{\gamma}{\gamma-1} n_1 T_1 V_{in1}$, with a similar relation for H_{in2}, where γ is the adiabatic index taken to be 5/3, and $T_{1,2}$ are the total temperatures at the inflow boundaries. Equation (8) becomes

$$dU_{th} = \frac{\frac{<H_x>}{<nV_x>} - \frac{\gamma}{\gamma-1} \frac{(n_1 T_1 V_{in1} + n_2 T_2 V_{in2})}{(n_1 V_{in1} + n_2 V_{in2})}}{\frac{(S_{in1} + S_{in2})}{(n_1 V_{in1} + n_2 V_{in2})}} \tag{10}$$

For the time when reconnection reaches a quasi-steady state and the reconnection electric field E_r is spatially uniform in the region of interest, we have $S_{in1} + S_{in2} = E_r(B_1 + B_2)/\mu_0$, where $B_{1,2}$ are $|B_x|$ at the inflow boundaries. In situations when the contribution from $E_x B_y$ can be neglected (e.g., with weak guide field), the inflow speeds can be approximated to be $V_{in1,2} = E_r/B_{1,2}$. Upon rearrangements of the terms, the rate of the thermal energy gain equation becomes

$$dU_{th,I} = \frac{\frac{<H_x>}{<nV_x>} - \frac{\gamma}{\gamma-1} T_{in}}{m_i V_{A,asym}^2} \tag{11}$$

where $T_{in} = \frac{n_1 T_1 B_2 + n_2 T_2 B_1}{n_1 B_2 + n_2 B_1}$ and $V_{A,asym} = \sqrt{\frac{B_1 B_2}{\mu_0 m_i} \frac{B_1 + B_2}{n_1 B_2 + n_2 B_1}}$.

If we further neglect the off-diagonal terms and the anisotropy of the pressure tensor in the outflow region, $H_x = \frac{\gamma}{\gamma-1} n V_x T$, and the equation evolves to

$$dU_{th,II} = \frac{\gamma}{\gamma-1} \frac{\frac{<nV_xT>}{<nV_x>} - T_{in}}{m_i V_{A,asym}^2} \qquad (12)$$

The first term is the weighted average of the temperature with the weighting factor to be nV_x. If we replace the weighted average with a simpler form, $<nV_xT> = <nV_x> <T>$, under the assumption that nV_x is independent of the z position, the formula becomes that provided in Shay et al. (2014)

$$dU_{th,III} = \frac{\gamma}{\gamma-1} \frac{<T> - T_{in}}{m_i V_{A,asym}^2} \qquad (13)$$

In order to check how well the above approximate formulas can represent the thermal energy gain, we test these formulas for the simulation with $B_g = 0$. The results are shown in Figure 9 ((a) for electrons and (b) for ions) plotted as a function of x^*, where the ion edges are selected as the z boundaries of the analysis regions. The black curve represents the original formula for the thermal energy gain ratio (equation (8)). For electrons, it takes about 50% of the input electromagnetic energy in the EDR and reduces to quasi-steady 15–20% around the end of the IDR and beyond. Within a few d_i, the formula $dU_{th,II}$ using the average temperature weighted by nV_x (equation (12), blue curve) agrees well with the exact calculation, while $dU_{th,III}$ using the simple average provides much lower values (equation (13), green curve). At larger distances from the X-line, both approximated formulas underestimate the thermal energy gain ratio. It is confirmed that the discrepancy at large distances is mainly due to the assumption of $\partial/\partial t = 0$ and the usage of equation (9) to estimate the aspect ratio. At the selected time, the front of the reconnection structure is at ~13 d_i from the X-line, and the region within about 4 d_i reaches the quasi-steady state. In reality, if the reconnection develops for longer time and the front of the reconnection structure is pushed further away from the X-line, equation (12) may be valid for larger regions (confirmed by a test using data from later time $t\omega_{ci} = 72$ with the quasi-steady region extending to ~8 d_i). For simulation studies, if a steady state for larger regions is desired, simulations will need to have larger domains and run for longer time; boundary conditions other than conducting walls will be required to avoid running out of magnetic fluxes at later time. It is interesting that equation (13), although it provides lower values than the electron thermal energy gain ratio based on our definition, is relatively constant within 2–8% with a decrease from the diffusion region to downstream regions (green curve in Figure 8a). The value is similar to those shown in previous studies for magnetopause reconnection (4.3%; Phan et al., 2013), symmetric reconnection simulation (8.25%; Shay et al., 2014), and MRX experiments for asymmetric reconnection (12.25%; Yoo et al., 2017).

The test result is similar for the ion thermal energy gain ratio (Figure 9b). The exact calculation (black curve) suggests that the ion thermal energy gain ratio increases from ~0 close to the X-line to ~30% near the end of the IDR and further increases downstream. The approximate formula $dU_{th,I}$ (equation (11), red curve), which still keeps the off-diagonal terms and the anisotropy of the pressure tensor in the outflow region, reasonably agrees with the black curve within a few d_i; it underestimates the thermal energy gain ratio at larger distances, due to the assumption of $\partial/\partial t = 0$ and the usage of equation (9) to estimate the aspect ratio. Other approximations of using the average temperature (weighted by nV_x [equation (12), blue], weighted by n [orange], and without weighting [equation (13), green]) are not far from the result obtained by equation (11) but overall have larger discrepancies. A previous study applied an approximated formula for the ion thermal energy gain using the average temperature weighted by n (neglecting the V_x dependence on the z position) to magnetopause far exhaust observations, and obtained a result of 33% (Phan et al., 2014). For comparison, we tested the same approximated formula in our simulation, and the result is about 12% at large distances (orange curve), smaller than that in the observations.

The flow energy gains of electrons and ions are obtained using equation (4) normalized by U_{in}. Close to the end of the IDR and further downstream, the electron flow energy gain is negligible as expected (~1%), and the ion flow energy gain is about constant (15%). At such distances from the X-line, the calculated total energy gain by integrating $\mathbf{J}_i \cdot \mathbf{E}$ or $\mathbf{J}_e \cdot \mathbf{E}$ is well balanced with the sum of the flow and thermal energy gain; that is, the heat flux is negligible.
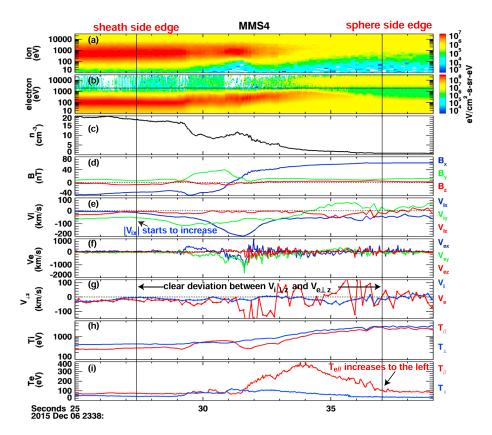
Figure 10. Energy partition for a diffusion region event observed by MMS. (a) Ion energy spectrogram, (b) electron energy spectrogram, (c) density, (d) magnetic field, (e) ion velocity, (f) electron velocity, (g) z component of the perpendicular velocity for ions (blue) and electrons (red), (h) ion temperature, and (i) electron temperature. Electron moments are calculated for <2 keV populations. The first vertical line marks the magnetosheath side ion edge, where $|V_{ix}|$ starts to increase (toward the right side). It is also the time when $V_{i\perp z}$ starts to deviate from $V_{e\perp z}$. The second vertical line represents the ion edge on the magnetospheric side, where $T_{e//}$ starts to increase (toward the left side) and is also at the time when $V_{i\perp z}$ starts to agree with $V_{e\perp z}$. The selected ion edges roughly represent the z boundaries of the ion diffusion region. The analysis results suggest comparable energy partition between ions and electrons for this event.

In summary, using the temperature change from the inflow to outflow regions with the weighting factor of nV_x (equation (12)) provides a reasonable estimate of the thermal energy gain ratio in the diffusion region (within a few d_i from the X-line) where the structure reaches a quasi-steady state in our $B_g = 0$ simulation test. The formulas work less well with increasing B_g, since the assumption of symmetric exhausts breaks, and the neglection of E_xB_y term for the inflow velocity introduces errors. We will next analyze an observation event with $B_g \sim 0.27$ at a few d_i from the X-line. The PIC test for $B_g = 0.2$ suggests that the electron and ion thermal energy gain ratios obtained from equations (11) and (12) differ from the real values by about 10%. Also note that all quantities in the formulas above are in the X-line frame, and hence, in the observations, the X-line motion needs to be estimated and all quantities need to be transformed to be in the X-line frame. We would like to mention that the simulation has the same temperatures on the two upstream sides, while at the dayside magnetopause, the magnetospheric side usually has a higher temperature. Further studies are required to know whether the temperature asymmetry would invalidate or improve the approximate formulas, or if it could cause a lower ion temperature increase in the simulation than in the observation study (Phan et al., 2014).

4. Observation Result of Energy Partition for a Diffusion Region Event

In this section, we show the energy partition analysis for a diffusion region event during magnetopause reconnection observed by MMS on 6 December 2015. The overview plot with measurements from MMS4 is shown in Figure 10. The spacecraft crossed the magnetopause from the magnetosheath to the

magnetospheric side as can be seen from the ion (Figure 10a) and electron (Figure 10b) spectrograms and the density profile (Figure 10c). Two electron populations with distinct energies exist on the magnetospheric side (Figure 10b, near the right end of the interval). The low-energy electrons in the magnetospheric inflow region may consist of ionospheric electrons and/or magnetosheath electrons transported to the magnetospheric side (e.g., see discussions in Wang et al., 2017). The high-energy population consists of ring current electrons. In the following analysis, we only consider the low-energy population, and the moments data are calculated for electrons below 2 keV. Magnetic field and velocity vectors are plotted in the xyz coordinate as in simulations (Figures 10d–10f). The current sheet normal is determined by the Minimum Directional Derivative method (Denton et al., 2016; Shi et al., 2005) along the direction of the maximum magnetic field gradient using four-spacecraft measurements during 23:38:29–23:38:32 UT. Selecting magnetic fields in the upstream intervals 23:38:23–23:38:24 UT on the magnetosheath side and 23:38:47–23:38:48 UT on the magnetospheric side, the bisection of the two magnetic field vectors projected to the plane perpendicular to the normal is used as the out-of-plane y direction. The x direction is then determined to complete the right-handed orthogonal xyz coordinate. In the GSM coordinate, x = [0.1113, −0.5579, 0.8224], y = [0.5288, 0.7339, 0.4263], and z = [−0.8414, 0.3874, 0.3767]. With such a coordinate, the guide field level is $|B_y/B_x|$ = 0.27. The spacecraft crossed the reconnection region on the −x side of the X-line with negative V_{ix} and V_{ex} jets. This event was suggested to be well inside the IDR based on the near-90-degree pitch angle distributions of magnetosheath ions close to their magnetospheric boundaries, due to the finite gyroradius effect of their meandering motion. By comparing the electron anisotropy in the exhaust with 2-D simulations, the observation location was suggested to be a few d_i from the X-line (Khotyaintsev et al., 2016). The x component of the electron perpendicular velocity well agrees with the $\mathbf{E} \times \mathbf{B}$ drift velocity in the outflow jet (shown in Figure 3 of Khotyaintsev et al., 2016), and electron distributions close to the B_x reversal exhibit a field-aligned beam (not shown) instead of meandering signatures such as counterstreaming populations along z (e.g., Figure 2 in Chen et al., 2016), suggesting that the observation location is outside the central EDR.

For estimating the energy partition quantities, we transform the velocities to the X-line frame. The normal velocity of the magnetopause is estimated by the timing analysis of B_x as −42 km/s. The X-line velocity tangential to the magnetopause is approximated to be the magnetosheath upstream V_{ix} = −5 km/s and V_{iy} = −73 km/s. The small V_x supports the event to be close to a crossing without much variation of the x location (an assumption in the analysis method discussed in section 3.4 in order to obtain equation (8)).

Next we select the z boundaries for the analysis, aiming to including most energized populations in the current sheet within the z boundaries and have particles mostly frozen-in at the inflow boundaries (to fulfill the assumption in section 3.4 that leads to equation (11)). The magnetosheath side separatrix is at about 23:38:29.2 UT, after which the bulk V_{ex} becomes positive due to magnetosheath electrons flowing toward the X-line, and the density decreases due to a loss of magnetosheath electrons that move away from the X-line. The first vertical line around 23:38:27.4 UT is selected as the magnetosheath side ion edge (on the inflow side of the separatrix). After the marked time, the amplitude of V_{ix} starts to increase due to existence of outflowing ions. On the magnetospheric side, the separatrix is inferred to be around 23:38:31.5 UT near the end of the V_{ex} jet. The magnetospheric side ion edge is selected to be at 23:38:37 UT (second vertical line), where $T_{e//}$ starts to increase toward the left, suggesting heating of magnetospheric inflow electrons in the IDR. The perpendicular velocities $V_{i\perp z}$ and $V_{e\perp z}$ have clear deviations between the two selected edges. The two velocities well agree with each other before the magnetosheath side edge; they become mostly matched after the magnetospheric side edge, although fluctuations remain due to lower hybrid type waves (waves spectra shown in Khotyaintsev et al., 2016). Such agreement between $V_{i\perp z}$ and $V_{e\perp z}$ suggests that ions and electrons are frozen-in and following the $\mathbf{E} \times \mathbf{B}$ drift outside the selected edges, and the edges also roughly represent the z boundaries of the IDR. The energy partition analysis is performed for each of the four spacecraft (average separation of 0.35 d_i based on the magnetosheath density of 20/cm^3).

According to the simulation test of the analysis method, we use the average temperature increase weighted by nV_x (equation (12)) to estimate the electron thermal energy gain ratio. The average result over the four spacecraft is 46.6%. The ion thermal energy gain ratio is estimated using equation (11), where off-diagonal terms and anisotropy of the pressure tensor are maintained for calculating the enthalpy flux. The ion thermal energy gain ratio between the ion edges averaged over spacecraft is 24.8%. Replacing H_x in equation (11) by the bulk flow energy flux and neglecting the input bulk flow energy flux, we obtain the electron flow energy

gain ratio ($dU_{Ke} = \left(< K_{ex} > / \left(< nV_{ex} > m_i V_{A,asym}^2 \right) \right)$) to be 1.8% and the ion flow energy gain ratio ($dU_{Ki} = \left(< K_{ix} > / \left(< nV_{ix} > m_i V_{A,asym}^2 \right) \right)$) to be 14.2%. Thus, the total electron energy gain ratio is 48.4%, which is about 1.25 times the ion energy gain ratio of 39.0%. The result suggests that ions and electrons have comparable energy partition for this event for the observed location, consistent with the simulation result for all guide field cases in the aspect that at a few d_i from the X-line (in the x direction) within the IDR, ions, and electrons have comparable energy partition (see Figures 2c and 2d).

5. Conclusions and Discussions

In this study, we use PIC simulations to investigate the energy partition during asymmetric reconnection in the diffusion region and discuss the energy conversion mechanisms by comparing the relative importance between the reconnection and in-plane electric fields. The effect of the guide field and the dependence on the distance from the X-line are emphasized. The energy partition is analyzed for a magnetopause reconnection event in the IDR using MMS observations. The main conclusions are as follows.

1. The partition of dissipated electromagnetic energies depends on the distance from the X-line of the integration region. Within the EDR, nearly all converted field energies go to electrons. From the EDR to the IDR scales, the energy deposition rate (relative to the input electromagnetic field energy available for conversion) to electrons decreases and that to ions increases. By the end of the IDR, the electron energy gain ratio reaches a constant rate of about 20%; the ion energy gain ratio is about 30–50% and continues to increase further downstream.

Such distance-dependent energy partition is consistent with the combined picture based on the previous studies at the far exhaust (Phan et al., 2013, 2014) and in the diffusion region about 2 d_i surrounding the X-line (Yamada et al., 2014; Yoo et al., 2017): the ion energy gain becomes more dominant with increasing distances from the X-line.

2. The analysis of the example MMS event shows comparable ion and electron energy gain, consistent with the presented simulation result in the transition from the EDR to the IDR.
3. With varying guide field (0 to 1 of the magnetosheath reconnecting component), the presented simulations do not exhibit much difference in the reconnection rate profiles. By selecting the time with the same reconnection rate, the guide field has little effect on the overall energy partition at the IDR scale and further downstream, except for creating asymmetry between two sides of the exhaust. Within the EDR, the guide field reduces the electron energy gain as well as the ratio between the electron and ion energy gain.
4. The ion energization within the x-extent of the EDR is mainly by the reconnection electric field. At larger scales, the relative importance between the reconnection and in-plane electric fields is time dependent: comparable near the peak reconnection rate, and more dominant by the in-plane electric fields at later time as the in-plane electric fields further develop. The major guide field effect is to make the relative importance between the reconnection and in-plane electric fields asymmetric in two sides of the exhaust.

The importance of in-plane electric fields in energizing ions in the diffusion region is consistent with previous studies. It is demonstrated by counterstreaming ion distributions for symmetric reconnection during magnetotail reconnection observations (e.g., Wygant et al., 2005) and hybrid simulations (Aunai et al., 2011b), as well as the 2-D profile in laboratory experiments (Yoo et al., 2014, 2017). The $\mathbf{J}_i \cdot \mathbf{E}$ in the laboratory experiment for asymmetric reconnection with zero guide field about 2 d_i from the X-line in the outflow direction is mainly enhanced on the magnetosheath side, which is close to the PIC simulation result (Figure 7a). Our PIC simulation result further shows that at 5–8 d_i from the X-line in the outflow direction, the $\mathbf{J}_i \cdot \mathbf{E}$ enhancements occur at both the magnetosheath and the magnetospheric sides.

5. The electron energization in the EDR is mainly by the reconnection electric field, which is reduced in a larger guide field due to the decrease of the current layer thickness. In-plane electric fields primarily do negative work on electrons, mainly at the end of the EDR and further downstream. Close to the X-line, in-plane electric fields provide positive contributions to energizing electrons. The contributions are reduced with sufficiently large guide fields due to the lack of accumulated energized electrons that increase the pressure near the X-line and due to the reduced distance between the X-line and the stagnation location.

Such reconnection-electric-field-dominant electron energy conversion differs from recent 2-D PIC simulation studies of asymmetric reconnection with zero guide field, where in-plane electric fields are shown to be dominant in energizing electrons in the EDR (Cassak et al., 2017; Swisdak et al., 2018). In their simulation results, the $\mathbf{J} \cdot \mathbf{E}$ profile exhibits large-amplitude oscillations due to oscillating V_{ez} near the magnetospheric side separatrix (Swisdak et al., 2018). In addition, $\mathbf{J} \cdot \mathbf{E}$ is clearly peaked on the magnetospheric side between the X-line and the stagnation point (Cassak et al., 2017), while it is relatively uniform along z for the $\mathbf{J} \cdot \mathbf{E}$ enhanced region in the simulation presented here. Comparing the simulation setups, the major difference is the upstream temperature conditions: a T_e ratio between the magnetospheric and magnetosheath side of 10.7 is applied in Swisdak et al. (2018) and Cassak et al. (2017) studies, while equal temperatures are used in simulations of the present study. Future studies are needed to know whether and how the temperature asymmetry affects the electron energization in the asymmetric reconnection EDR. As a reference, for the presented MMS event, the T_e ratio using the magnetospheric inflow T_e just upstream of the reconnection layer (at 23:38:37 UT in Figure 10) is 1.3 based on the T_e for electrons below 2 keV (these electrons take up 7/8 in density percentage and hence may dominate the dynamics in the inflow region) and 6.7 using the T_e for electrons in the entire energy range (0–30 keV).

How the upstream conditions such as the temperature asymmetry may influence the energy partition remains an open question. To make progress toward answering this question, we will need better assessment on the following: what is the true upstream condition that controls the dayside reconnection? The far upstream magnetosphere (tens of d_i away from the magnetopause) typically has a temperatures about an order of magnitude higher than that in the magnetosheath. On the other hand, during 3-D reconnection, turbulence develops in an $\sim d_i$ scale layer near the magnetospheric side separatrix and enables transport of exhaust particles (colder than particles in the far magnetosphere upstream) to the magnetospheric side inflow region (e.g., Graham et al., 2016; Le et al., 2017) such as in the MMS event shown in Figure 10 (Wang et al., 2017). In addition, a boundary layer has been shown to exist in the magnetospheric side inflow region close to the magnetopause (e.g., in the event shown in Figure 10, after ~23:38:37 UT), consisting of cold ionospheric electrons and/or magnetosheath electrons transported to the magnetosphere during earlier reconnection, and these low-energy particles may serve as inflow populations for the ongoing reconnection. Thus, the immediate upstream on the magnetospheric side, for example, on the order of a few d_i, may have a much lower electron temperature than that further into the magnetosphere and thus resulting in more symmetric upstream temperatures like in the presented event (Figure 10). Therefore, further understanding of 3-D effects and the large-scale dayside magnetosphere structure is needed to address the question of the true upstream condition and the effect of the upstream condition on energy partition.

References

Aunai, N., Belmont, G., & Smets, R. (2011a). Energy budgets in collisionless magnetic reconnection: Ion heating and bulk acceleration. *Physics of Plasmas*, *18*(12), 122901. https://doi.org/10.1063/1.3664320

Aunai, N., Belmont, G., & Smets, R. (2011b). Proton acceleration in antiparallel collisionless magnetic reconnection: Kinetic mechanisms behind the fluid dynamics. *Journal of Geophysical Research*, *116*, A09232. https://doi.org/10.1029/2011JA016688

Birn, J., Borovsky, J. E., Hesse, M., & Schindler, K. (2010). Scaling of asymmetric reconnection in compressible plasmas. *Physics of Plasmas*, *17*(5), 052108. https://doi.org/10.1063/1.3429676

Birn, J., & Hesse, M. (2005). Energy release and conversion by reconnection in the magnetotail. *Annales Geophysicae*, *23*(10), 3365–3373. https://doi.org/10.5194/angeo-23-3365-2005

Birn, J., & Hesse, M. (2010). Energy release and transfer in guide field reconnection. *Physics of Plasmas*, *17*(1), 012109. https://doi.org/10.1063/1.3299388

Bowers, K. J., Albright, B. J., Yin, L., Bergen, B., & Kwan, T. J. T. (2008). Ultrahigh performance three-dimensional electromagnetic relativistic kinetic plasma simulation. *Physics of Plasmas*, *15*(5), 055703. https://doi.org/10.1063/1.2840133

Burch, J. L., Moore, T. E., Torbert, R. B., & Giles, B. L. (2016). Magnetospheric multiscale overview and science objectives. *Space Science Reviews*, *199*, 5–21. https://doi.org/10.1007/s11214-015-0164-9

Burch, J. L., Torbert, R. B., Phan, T. D., Chen, L.-J., Moore, T. E., Ergun, R. E., et al. (2016). Electron-scale measurements of magnetic reconnection in space. *Science*, *352*(6290), aaf2939. https://doi.org/10.1126/science.aaf2939

Cassak, P. A., Genestreti, K. J., Burch, J. L., Phan, T.-D., Shay, M. A., Swisdak, M., et al. (2017). The effect of a guide field on local energy conversion during asymmetric magnetic reconnection: Particle-in-cell simulations. *Journal of Geophysical Research: Space Physics*, *122*, 11,523–11,542. https://doi.org/10.1002/2017JA024555

Chen, L.-J., Daughton, W. S., Lefebvre, B., & Torbert, R. B. (2011). The inversion layer of electric fields and electron phase-space-hole structure during two-dimensional collisionless magnetic reconnection. *Physics of Plasmas*, *18*(1), 012904. https://doi.org/10.1063/1.3529365

Chen, L.-J., Hesse, M., Wang, S., Bessho, N., & Daughton, W. (2016). Electron energization and structure of the diffusion region during asymmetric reconnection. *Geophysical Research Letters*, *43*, 2405–2412. https://doi.org/10.1002/2016GL068243

Chen, L.-J., Hesse, M., Wang, S., Gershman, D., Ergun, R., Pollock, C., et al. (2016). Electron energization and mixing observed by MMS in the vicinity of an electron diffusion region during magnetopause reconnection. *Geophysical Research Letters*, *43*, 6036–6043. https://doi.org/10.1002/2016GL069215

Dahlin, J. T., Drake, J. F., & Swisdak, M. (2014). The mechanisms of electron heating and acceleration during magnetic reconnection. *Physics of Plasmas*, *21*(9), 092304. https://doi.org/10.1063/1.4894484

Dahlin, J. T., Drake, J. F., & Swisdak, M. (2015). Electron acceleration in three-dimensional magnetic reconnection with a guide field. *Physics of Plasmas*, *22*(10), 100704. https://doi.org/10.1063/1.4933212

Dahlin, J. T., Drake, J. F., & Swisdak, M. (2016). Parallel electric fields are inefficient drivers of energetic electrons in magnetic reconnection. *Physics of Plasmas*, *23*(12), 120704. https://doi.org/10.1063/1.4972082

Denton, R. E., Sonnerup, B. U. Ö., Hasegawa, H., Phan, T. D., Russell, C. T., Strangeway, R. J., et al. (2016). Motion of the MMS spacecraft relative to the magnetic reconnection structure observed on 16 October 2015 at 1307 UT. *Geophysical Research Letters*, *43*, 5589–5596. https://doi.org/10.1002/2016GL069214

Drake, J. F., Cassak, P. A., Shay, M. A., Swisdak, M., & Quataert, E. (2009). A magnetic reconnection mechanism for ion acceleration and abundance enhancements in impulsive flares. *The Astrophysical Journal*, *700*(1), L16–L20. https://doi.org/10.1088/0004-637X/700/1/L16

Eastwood, J. P., Phan, T. D., Drake, J. F., Shay, M. A., Borg, A. L., Lavraud, B., & Taylor, M. G. G. T. (2013). Energy partition in magnetic reconnection in Earth's magnetotail. *Physical Review Letters*, *110*(22), 225001. https://doi.org/10.1103/PhysRevLett.110.225001

Fu, S., Huang, S., Zhou, M., Ni, B., & Deng, X. (2018). Tripolar electric field structure in guide field magnetic reconnection. *Annales de Geophysique*, *36*(2), 373–379. https://doi.org/10.5194/angeo-36-373-2018

Fu, X.-R., Lu, Q.-M., & Wang, S. (2006). The process of electron acceleration during collionless magnetic reconnection. *Physics of Plasmas*, *13*(1), 012309. https://doi.org/10.1063/1.2164808

Fujimoto, K. (2014). Wave activities in separatrix regions of magnetic reconnection. *Geophysical Research Letters*, *41*, 2721–2728. https://doi.org/10.1002/2014GL059893

Graham, D. B., Khotyaintsev, Y. V., Norgren, C., Vaivads, A., André, M., Toledo-Redondo, S., et al. (2016). Lower hybrid waves in the ion diffusion and magnetospheric inflow regions. *Journal of Geophysical Research: Space Physics*, *122*, 517–533. https://doi.org/10.1002/2016JA023572

Guo, X., Horiuchi, R., Cheng, C. Z., Kaminou, Y., & Ono, Y. (2017). Energy conversion mechanism for electron perpendicular energy in high guide-field reconnection. *Physics of Plasmas*, *24*(3), 032901. https://doi.org/10.1063/1.4977908

Haggerty, C. C., Shay, M. A., Drake, J. F., Phan, T. D., & McHugh, C. T. (2015). The competition of electron and ion heating during magnetic reconnection. *Geophysical Research Letters*, *42*, 9657–9665. https://doi.org/10.1002/2015GL065961

Hesse, M., Aunai, N., Zenitani, S., Kuznetsova, M., & Birn, J. (2013). Aspects of collisionless magnetic reconnection in asymmetric systems. *Physics of Plasmas*, *20*(6), 061210. https://doi.org/10.1063/1.4811467

Hesse, M., Chen, L.-J., Liu, Y.-H., Bessho, N., & Burch, J. L. (2017). Population mixing in asymmetric magnetic reconnection with a guide field. *Physical Review Letters*, *118*(14), 145101. https://doi.org/10.1103/PhysRevLett.118.145101

Hesse, M., Liu, Y.-H., Chen, L.-J., Bessho, N., Kuznetsova, M., Birn, J., & Burch, J. L. (2016). On the electron diffusion region in asymmetric reconnection with a guide magnetic field. *Geophysical Research Letters*, *43*, 2359–2364. https://doi.org/10.1002/2016GL068373

Huang, C., Lu, Q., & Wang, S. (2010). The mechanisms of electron acceleration in antiparallel and guide field magnetic reconnection. *Physics of Plasmas*, *17*(7), 072306. https://doi.org/10.1063/1.3457930

Karimabadi, H., Daughton, W., & Scudder, J. (2007). Multi-scale structure of the electron diffusion region. *Geophysical Research Letters*, *34*, L13104. https://doi.org/10.1029/2007GL030306

Khotyaintsev, Y. V., Graham, D. B., Norgren, C., Eriksson, E., Li, W., Johlander, A., et al. (2016). Electron jet of asymmetric reconnection. *Geophysical Research Letters*, *43*, 5571–5580. https://doi.org/10.1002/2016GL069064

Kleva, R. G., Drake, J. F., & Waelbroeck, F. L. (1995). Fast reconnection in high temperature plasmas. *Physics of Plasmas*, *2*(1), 23–34. https://doi.org/10.1063/1.871095

Le, A., Daughton, W., Chen, L.-J., & Egedal, J. (2017). Enhanced electron mixing and heating in 3-D asymmetric reconnection at the Earth's magnetopause. *Geophysical Research Letters*, *44*, 2096–2104. https://doi.org/10.1002/2017GL072522

Li, X.-C., Guo, F., Li, H., & Li, G. (2015). Nonthermally dominated electron acceleration during magnetic reconnection in a low-β plasma. *The Astrophysical Journal Letters*, *811*(2), L24. https://doi.org/10.1088/2041-8205/811/2/L24

Liu, Y.-H., Daughton, W., Karimabadi, H., Li, H., & Gary, S. P. (2014). Do dispersive waves play a role in collisionless magnetic reconnection? *Physics of Plasmas*, *21*(2), 022113. https://doi.org/10.1063/1.4865579

Liu, Y. H., Mouikis, C. G., Kistler, L. M., Wang, S., Roytershteyn, V., & Karimabadi, H. (2015). The heavy ion diffusion region in magnetic reconnection in the Earth's magnetotail. *Journal of Geophysical Research: Space Physics*, *120*, 3535–3551. https://doi.org/10.1002/2015JA020982

Lu, S., Angelopoulos, V., & Fu, H. (2016). Suprathermal particle energization in dipolarization fronts: Particle-in-cell simulations. *Journal of Geophysical Research: Space Physics*, *121*, 9483–9500. https://doi.org/10.1002/2016JA022815

Lu, S., Lu, Q., Huang, C., & Wang, S. (2013). The transfer between electron bulk kinetic energy and thermal energy in collionless magnetic reconnection. *Physics of Plasmas*, *20*(6), 061203. https://doi.org/10.1063/1.4811119

Lu, S., Pritchett, P. L., Angelopoulos, V., & Artemyev, A. V. (2018). Magnetic reconnection in Earth's magnetotail: Energy conversion and its earthward-tailward asymmetry. *Physics of Plasmas*, *25*(1), 012905. https://doi.org/10.1063/1.5016435

Nagai, T., Shinohara, I., & Zenitani, S. (2015). Ion acceleration processes in magnetic reconnection: Geotail observations in the magnetotail. *Journal of Geophysical Research: Space Physics*, *120*, 1766–1783. https://doi.org/10.1002/2014JA020737

Øieroset, M., Phan, T. D., Haggerty, C., Shay, M. A., Eastwood, J. P., Gershman, D. J., et al. (2016). MMS observations of large guide field symmetric reconnection between colliding reconnection jets at the center of a magnetic flux rope at the magnetopause. *Geophysical Research Letters*, *43*, 5536–5544. https://doi.org/10.1002/2016GL069166

Phan, T. D., Drake, J. F., Shay, M. A., Gosling, J. T., Paschmann, G., Eastwood, J. P., et al. (2014). Ion bulk heating in magnetic reconnection exhausts at Earth's magnetopause: Dependence on the inflow Alfvén speed and magnetic shear angle. *Geophysical Research Letters*, *41*, 7002–7010. https://doi.org/10.1002/2014GL061547

Phan, T. D., Shay, M. A., Gosling, J. T., Fujimoto, M., Drake, J. F., Paschmann, G., et al. (2013). Electron bulk heating in magnetic reconnection at Earth's magnetopause: Dependence on the inflow Alfvén speed and magnetic shear. *Geophysical Research Letters*, *40*, 4475–4480. https://doi.org/10.1002/grl.50917

Pollock, C., Moore, T., Jacques, A., Burch, J., Gliese, U., Saito, Y., et al. (2016). Fast plasma investigation for magnetospheric multiscale. *Space Science Reviews*, *199*(1-4), 331–406. https://doi.org/10.1007/s11214-016-0245-4

Pritchett, P. L. (2008). Collisionless magnetic reconnection in an asymmetric current sheet. *Journal of Geophysical Research*, *113*, A06210. https://doi.org/10.1029/2007JA012930

Pritchett, P. L., & Coroniti, F. V. (2004). Three-dimensional collisionless magnetic reconnection in the presence of a guide field. *Journal of Geophysical Research*, *109*, A01220. https://doi.org/10.1029/2003JA009999

Pritchett, P. L., & Mozer, F. S. (2009). Asymmetric magnetic reconnection in the presence of a guide field. *Journal of Geophysical Research*, *114*, A11210. https://doi.org/10.1029/2009JA014343

Russell, C. T., Anderson, B. J., Baumjohann, W., Bromund, K. R., Dearborn, D., Fischer, D., et al. (2016). The Magnetospheric multiscale magnetometers. *Space Science Reviews*, *199*(1-4), 189–256. https://doi.org/10.1007/s11214-014-0057-3

Shay, M. A., Haggerty, C. C., Phan, T. D., Drake, J. F., Cassak, P. A., & Wu, P., et al. (2014). Electron heating during magnetic reconnection: A simulation scaling study. *Physics of Plasmas*, *21*(12), 122902. https://doi.org/10.1063/1.4904203

Shay, M. A., Phan, T. D., Haggerty, C. C., Fujimoto, M., Drake, J. F., Malakit, K., et al. (2016). Kinetic signatures of the region surrounding the X line in asymmetric (magnetopause) reconnection. *Geophysical Research Letters*, *43*, 4145–4154. https://doi.org/10.1002/2016GL069034

Shi, Q. Q., Shen, C., Pu, Z. Y., Dunlop, M. W., Zong, Q.-G., Zhang, H., et al. (2005). Dimensional analysis of observed structures using multipoint magnetic field measurements: Application to Cluster. *Geophysical Research Letters*, *32*, L12105. https://doi.org/10.1029/2005GL022454

Shuster, J. R., Chen, L.-J., Hesse, M., Argall, M. R., Daughton, W., Torbert, R. B., & Bessho, N. (2015). Spatiotemporal evolution of electron characteristics in the electron diffusion region of magnetic reconnection: Implications for acceleration and heating. *Geophysical Research Letters*, *42*, 2586–2593. https://doi.org/10.1002/2015GL063601

Sitnov, M. I., Swisdak, M., & Divin, A. V. (2009). Dipolarization fronts as a signature of transient reconnection in the magnetotail. *Journal of Geophysical Research*, *114*, A04202. https://doi.org/10.1029/2008JA013980

Swisdak, M., Drake, J. F., Price, L., Burch, J. L., Cassak, P. A., & Phan, T.-D. (2018). Localized and intense energy conversion in the diffusion region of asymmetric magnetic reconnection. *Geophysical Research Letters*, *45*, 5260–5267. https://doi.org/10.1029/2017GL076862

Swisdak, M., Rogers, B. N., Drake, J. F., & Shay, M. A. (2003). Diamagnetic suppression of component magnetic reconnection at the magnetopause. *Journal of Geophysical Research*, *108*(A5), 1218. https://doi.org/10.1029/2002JA009726

Tyler, E., Cattell, C., Thaller, S., Wygant, J., Gurgiolo, C., Goldstein, M., & Mouikis, C. (2016). Partitioning of integrated energy fluxes in four tail reconnection events observed by Cluster. *Journal of Geophysical Research: Space Physics*, *121*, 11,798–11,825. https://doi.org/10.1002/2016JA023330

Wang, H., Lu, Q., Huang, C., & Wang, S. (2016). The mechanisms of electron acceleration during multiple X line magnetic reconnection with a guide field. *The Astrophysical Journal*, *821*(2), 84. https://doi.org/10.3847/0004-637X/821/2/84

Wang, H., Lu, Q., Huang, C., & Wang, S. (2017). Electron acceleration in a secondary magnetic island formed during magnetic reconnection with a guide field. *Physics of Plasmas*, *24*(5), 052113. https://doi.org/10.1063/1.4982813

Wang, S., Chen, L. J., Hesse, M., Wilson, L. B. III, Bessho, N., Gershman, D. J., et al. (2017). Parallel electron heating in the magnetospheric inflow region. *Geophysical Research Letters*, *44*, 4384–4392. https://doi.org/10.1002/2017GL073404

Werner, G. R., & Uzdensky, D. A. (2017). Nonthermal particle acceleration in 3D relativistic magnetic reconnection in pair plasma. *Astrophys. J. Lett.*, *843*(2), L27. https://doi.org/10.3847/2041-8213/aa7892

Willis, D. M. (1971). Structure of the magnetopause. *Reviews of Geophysics*, *9*(4), 953–985. https://doi.org/10.1029/RG009i004p00953

Wygant, J. R., Cattell, C. A., Lysak, R., Song, Y., Dombeck, J., McFadden, J., et al. (2005). Cluster observations of an intense normal component of the electric field at a thin reconnecting current sheet in the tail and its role in the shock-like acceleration of the ion fluid into the separatrix region. *Journal of Geophysical Research*, *110*, A09206. https://doi.org/10.1029/2004JA010708

Yamada, M., Yoo, J., Jara-Almonte, J., Ji, H., Kulsrud, R. M., & Myers, C. E. (2014). Conversion of magnetic energy in the magnetic reconnection layer of a laboratory plasma. *Nature Communications*, *5*, 4474.

Yamada, M., Yoo, J., & Myers, C. E. (2016). Understanding the dynamics and energetics of magnetic reconnection in a laboratory plasma: Review of recent progress on selected fronts. *Physics of Plasmas*, *23*(5), 055402. https://doi.org/10.1063/1.4948721

Yoo, J., Na, B., Jara-Almonte, J., Yamada, M., Ji, H., Roytershteyn, V., et al. (2017). Electron heating and energy inventory during asymmetric reconnection in a laboratory plasma. *Journal of Geophysical Research: Space Physics*, *122*, 9264–9281. https://doi.org/10.1002/2017JA024152

Yoo, J., Yamada, M., Ji, H., Jara-Almonte, J., & Myers, C. E. (2014). Bulk ion acceleration and particle heating during magnetic reconnection in a laboratory plasma. *Physics of Plasmas*, *21*(5), 055706. https://doi.org/10.1063/1.4874331

Zenitani, S., Hesse, M., Klimas, A., & Kuznetsova, M. (2011). New measure of the dissipation region in collisionless magnetic reconnection. *Physical Review Letters*, *106*(19), 195003. https://doi.org/10.1103/PhysRevLett.106.195003